

Hybridization between chiral nutation modes in ferrimagnets

Yihang Duan(段懿航) and Ka Shen(沈卡)

Citation: Chin. Phys. B, 2026, 35 (**4**): 047504. DOI: 10.1088/1674-1056/ae3c8c
http://cpb.iphy.ac.cn; http://iopscience.iop.org/cpb

What follows is a list of articles you may be interested in

Tunable anomalous Hall effect and anisotropic magnetism in In-doped $TbMn_6Sn_6$ kagome magnets

Detong Wu(吴德桐), Jianwei Qin(秦建伟), and Bing Shen(沈冰)
Chin. Phys. B, 2025, 34 (**10**): 107511. DOI: 10.1088/1674-1056/adde37

Tailoring-compensated ferrimagnetic state and anomalous Hall effect in quaternary Mn-Ru-V-Ga Heusler compounds

Jin-Jing Liang(梁瑾静), Xue-Kui Xi(郗学奎), Wen-Hong Wang(王文洪), and Yong-Chang Lau(刘永昌)
Chin. Phys. B, 2024, 33 (**7**): 077504. DOI: 10.1088/1674-1056/ad34c8

Crystal growth, magnetic and electrical transport properties of the kagome magnet RCr_6Ge_6 (R=Gd-Tm)

Xingyu Yang(杨星宇), Qingqi Zeng(曾庆祺), Miao He(何苗), Xitong Xu(许锡童), Haifeng Du(杜海峰), and Zhe Qu(屈哲)
Chin. Phys. B, 2024, 33 (**7**): 077501. DOI: 10.1088/1674-1056/ad3dcf

Anomalous Hall effect in ferromagnetic $LaCo_2As_2$ and ferrimagnetic $NdCo_2As_2$

Yu-Qing Huang(黄雨晴), Peng-Yu Zheng(郑鹏宇), Rui Liu(刘瑞), Xi-Tong Xu(许锡童), Zi-Yang Wu(吴紫阳), Chao Dong(董超), Jun-Feng Wang(王俊峰), Zhi-Ping Yin(殷志平), and Shuang Jia(贾爽)
Chin. Phys. B, 2023, 32 (**10**): 107502. DOI: 10.1088/1674-1056/acd925

Ultrafast antiferromagnet rearrangement in Co/IrMn/CoGd trilayers

Zongxia Guo(郭宗夏), Gregory Malinowski, Pierre Vallobra, Yi Peng(彭懿), Yong Xu(许涌), Stéphane Mangin, Weisheng Zhao(赵巍胜), Michel Hehn, and Boyu Zhang(张博宇)
Chin. Phys. B, 2023, 32 (**8**): 087507. DOI: 10.1088/1674-1056/acda83

SPECIAL TOPIC — Advanced magnonics

Hybridization between chiral nutation modes in ferrimagnets

Yihang Duan(段懿航)[1,2] and Ka Shen(沈卡)[1,2,†]

[1] *The Center for Advanced Quantum Studies and School of Physics and Astronomy, Beijing Normal University, Beijing* 100875, *China*
[2] *Key Laboratory of Multiscale Spin Physics, Ministry of Education, Beijing Normal University, Beijing* 100875, *China*

(Received 19 November 2025; revised manuscript received 5 January 2026; accepted manuscript online 23 January 2026)

The hybridization between ferrimagnetic magnons of different chiralities holds potentials for applications in the design of magnonic devices. Whereas the nutation mode observed in the ferromagnetic film also possesses opposite chirality to precessional magnon mode, in the present work, we study the interplay of the nutation modes and chiral magnons in ferrimagnets with both parallel and antiparallel magnetic configurations based on the inertial Landau–Lifshitz–Gilbert equation. While the two configurations show some general features, such as the individual excitation of the nutation modes and the repulsion between nutation modes and conventional modes, the antiparallel configuration also exhibits a hybridization between two nutation modes and distinct dissipation behaviors, compared to the parallel configuration. A theoretical mode analysis was performed based on a perturbation approach, which nicely reproduces the observations in the simulation and clarifies the key role of the magnetic anisotropy in mode hybridization. Our findings offer a more comprehensive understanding of inertial effects in ferrimagnets, and could be useful for understanding experimental studies on ferrimagnets with non-negligible magnetic inertia.

Keywords: ferrimagnet, nutation, magnon, hybridization

PACS: 75.50.Gg, 75.78.–n, 76.50.+g, 75.30.Gw

DOI: 10.1088/1674-1056/ae3c8c **CSTR:** 32038.14.CPB.ae3c8c

1. Introduction

Antiferromagnets (AFMs) and ferrimagnets (FiMs) have recently attracted considerable research interest in the field of magnonics,[1,2] as they intrinsically host both left- and right-handed magnon modes, providing an additional chiral degree of freedom that can be linked to a variety of intriguing properties in strong magnon–phonon coupling,[3,4] magnon–photon interactions,[5] distinct magnon transmission in heterostructure,[6,7] etc. Compared to AFMs, the chiral magnon in FiMs can be more efficiently controlled and modulated through, for instance, an external magnetic field,[8,9] temperature,[10–14] or an electric field,[15,16] and therefore is believed to be a promising ingredient for designing novel magnonic devices such as magnonic logic computing[17,18] and unidirectional signal processing components.[19]

As quanta of spin waves, magnons in AFMs and FiMs are commonly described by the classical Landau–Lifshitz–Gilbert (LLG) equation of normalized sublattice magnetization $\boldsymbol{m}_i = \boldsymbol{M}_i/M_i$[20,21]

$$\frac{\mathrm{d}\boldsymbol{m}_i}{\mathrm{d}t} = -\gamma \boldsymbol{m}_i \times \boldsymbol{B}_i^{\mathrm{eff}} + \alpha' \boldsymbol{m}_i \times \frac{\mathrm{d}\boldsymbol{m}_i}{\mathrm{d}t}, \tag{1}$$

where the first and second terms correspond to magnetization precession around the effective field $\boldsymbol{B}_i^{\mathrm{eff}}$ and the magnetic damping parameterized by Gilbert damping constant α', respectively. Equation (1) is based on the conventional gyromagnetic relation $\boldsymbol{L}_i = \boldsymbol{M}_i/\gamma$, indicating the collinear alignment of the angular momentum and magnetization, which however might deviate when the angular momentum relaxation of the magnetic system becomes comparable to or even slower than the magnetization dynamics characterized by magnon frequency.[22–25] Such a feature can be captured by an extension of Eq. (1) to the so-called inertial Landau–Lifshitz–Gilbert (ILLG) equation as[26,27]

$$\frac{\mathrm{d}\boldsymbol{m}_i}{\mathrm{d}t} = -\gamma \boldsymbol{m}_i \times \boldsymbol{B}_i^{\mathrm{eff}} + \alpha' \boldsymbol{m}_i \times \left(\frac{\mathrm{d}\boldsymbol{m}_i}{\mathrm{d}t} + \tau \frac{\mathrm{d}^2 \boldsymbol{m}_i}{\mathrm{d}t^2} \right), \tag{2}$$

where the angular momentum relaxation time τ also refers to the inertial coefficient. As a result, instead of the simple precession, the magnetization exhibits nutation as depicted in Fig. 1. While theoretical studies have explored various characteristics of nutation in magnetic resonance,[26,28–31] as well as the volume[32–34] and surface spin waves,[35] the experimental observations of nutation dynamics via the time-resolved magneto-optical Kerr effect have also been reported in ferromagnetic (FM) films of CoFeB,[36] cobalt[37] and permalloy,[36,38] although not yet in AFMs and FiMs. According to Fig. 1, the nutation dynamics can be regarded as a superposition of the primary precession mode and a high-frequency nutation mode with opposite chirality. This implies that the nutation may considerably enrich the chiral magnetization dynamics particularly in FiMs, which naturally host primary field-sensitive precession modes of both chiralities.

[†]Corresponding author. E-mail: kashen@bnu.edu.cn

© 2026 Chinese Physical Society and IOP Publishing Ltd. All rights, including for text and data mining, AI training, and similar technologies, are reserved.

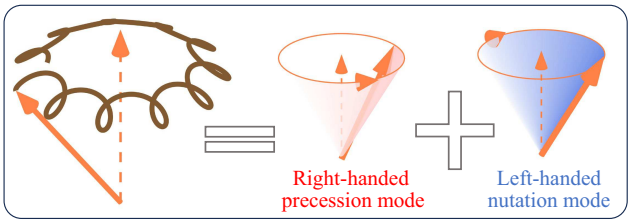


Fig. 1. The dynamics of a magnetic moment in a ferromagnet, when including nutation, comprises a right-handed precession mode and a left-handed nutation mode.

Whereas the nutation due to magnetic inertia has been proposed in FiMs,[26] in this work, we study the role of a magnetic field on the interplay between nutation and precession modes, as well as the mode hybridization, based on numerical solutions of the ILLG equation, where each precession mode is found to be accompanied by one nutation mode with opposite chirality. The magnetic field dependence of nutation frequencies is found to follow their primary precession modes qualitatively in both weak and strong exchange limits between the two sublattices, where an external magnetic field stabilizes a parallel configuration and an antiparallel one, respectively. Mode analysis reveals that, while nutation modes in the parallel configuration still comprise optical and acoustic modes, similar to the precession modes, they do not inherit the out-of-phase sublattice dynamics of the precession modes in the antiparallel configuration but exhibit the in-phase motion of magnetic moments. We also develop a perturbation approach to describe the mode hybridization and quantitatively evaluate the anticrossing gap.

The rest of this article is organized as follows. In Section 2, we introduce the macromagnetic model of FiM and our simulation method. The main results for the parallel and antiparallel configurations are presented and analyzed in Sections 3 and 4, respectively. A short summary is given in Section 5.

2. Model

We adopt a minimal model consisting of two antiferromagnetically coupled sublattices and introduce an easy-plane anisotropy to capture the demagnetization effect in film geometry. Focusing on the uniform modes in ferrimagnetic resonance, we take macromagnetic moments $\boldsymbol{M}_a$ and $\boldsymbol{M}_b$ for different sublattices and write the Hamiltonian as

$$H = -J\boldsymbol{M}_a \cdot \boldsymbol{M}_b - \sum_{i=a,b}\left[K_i\left(M_i^z\right)^2 + \mu_0 \boldsymbol{H}_{\rm ext}\cdot\boldsymbol{M}_i\right], \quad (3)$$

where $J<0$ corresponds to an antiferromagnetic coupling, $K_i<0$ the effective easy-plane anisotropy parameter, and $\mu_0\boldsymbol{H}_{\rm ext}$ the external magnetic field. The magnetic ground state is then determined by the minimum of Eq. (3) and the magnetic dynamics in the presence of a driving field $\boldsymbol{h}(t)$ is simulated by numerically solving the ILLG equation [Eq. (2)] with the instantaneous effective magnetic fields

$$\boldsymbol{B}_{a(b)}^{\rm eff} = J\boldsymbol{M}_{b(a)} + 2K_{a(b)}M_{a(b)}^z\hat{z} + \mu_0(\boldsymbol{H}_{\rm ext}+\boldsymbol{h}). \quad (4)$$

For the sake of computational procedures at $\tau\neq 0$, we rewrite Eq. (2) as

$$\frac{{\rm d}\boldsymbol{m}_i}{{\rm d}t} = \boldsymbol{g}_i/\eta, \quad (5)$$

$$\frac{{\rm d}\boldsymbol{g}_i}{{\rm d}t} = \gamma\boldsymbol{m}_i\times\left(\boldsymbol{B}_i^{\rm eff}\times\boldsymbol{m}_i\right) - (\alpha'\boldsymbol{g}_i + g_i^2\boldsymbol{m}_i + \boldsymbol{m}_i\times\boldsymbol{g}_i)/\eta, \quad (6)$$

with $\eta=\alpha'\tau$. For comparison, the conventional precession modes are also simulated at $\tau=0$ from an equivalent form of Eq. (1) as

$$\frac{{\rm d}\boldsymbol{m}_i}{{\rm d}t} = -\frac{\gamma}{1+\alpha'^2}\boldsymbol{m}_i\times\left(\boldsymbol{B}_i^{\rm eff}+\alpha'\boldsymbol{m}_i\times\boldsymbol{B}_i^{\rm eff}\right). \quad (7)$$

The fourth-order Runge–Kutta method is adopted in the present numerical simulation. The external dc magnetic field $\mu_0\boldsymbol{H}_{\rm ext}$ is set along the y direction throughout this paper.

3. Parallel configuration

Inspired by the experimental confirmation of magnetic inertia effect in FMs,[36–38] in this section, we consider a synthetic FiM system experimentally feasible by stacking two FM layers, where the two layers are antiferromagnetically coupled via the Ruderman–Kittel–Kasuya–Yoshida (RKKY) interaction across a nonmagnetic spacer layer, as illustrated in Fig. 2(a). Specifically, we take parameters in a permalloy-based FiM with $K_a=K_b=-0.05T/\mu_{\rm B}$, $\alpha'=0.023$[36] and $J=-0.02T/\mu_{\rm B}$.[39] The magnitudes of macromagnetic moments are controllable by the relative thickness of the two layers. Here we adopt effective values of $M_b=5\mu_{\rm B}$ and $M_a=3M_b$. Since the exchange field due to RKKY strength is around 0.1 T, which is too weak to stabilize an antiparallel alignment of the two macromagnetic moments under an external magnetic field in the range of $\mu_0 H_{\rm ext}\geq 1T$ applied in the simulation, the system is thus driven into a parallel configuration.

3.1. Nutation modes revealed by excitation via alternating fields

Starting from the conventional ferromagnetic resonance without the inertial term, i.e., $\tau=0$, we use a sinusoidal excitation magnetic field $\boldsymbol{h}(t)=h_0\sin(2\pi f_{\rm ac}t)\hat{x}$ with $\mu_0 h_0=1$ mT to excite the synthetic FiM. The amplitude of M_b^z in the steady state is plotted as a function of $\mu_0 H_{\rm ext}$ in Fig. 2(b) at different excitation frequencies. Two resonance peaks are observed at each excitation frequency, reflecting the existence of two magnon modes. Both resonance fields increase with $f_{\rm ac}$, as expected in the parallel configuration of FiM, where the two magnon modes correspond to the in-phase and out-of-phase precession of the two layers.[40]

When the inertial term is included with $\tau = 12$ ps,[36] the occurrence of nutation makes the amplitude of M_b^z vary with time even in a steady state. The maximal amplitudes are plotted in Fig. 2(c), which differ significantly from Fig. 2(b) without inertia. For an intuitive comparison, the resonance fields of the pure precession modes are extracted in Fig. 2(b) and plotted as dashed curves in Fig. 2(c). The two resonance fields with and without inertia are close to each other in the low-frequency range, reflecting the marginal role of inertia. When the frequency increases, the resonance peaks from the ILLG equation gradually deviate from the pure precession modes and shift to a larger magnetic field. Further increasing f_{ac} gives rise to two additional resonances, as denoted by blue triangles, with their resonance fields also moving toward larger values with higher excitation frequency. Since the conventional precession modes are not excited at these resonances, these additional peaks imply the emergence of nutation modes, as we will explicitly analyze below. Figure 2(c) thus indicates that the nutation modes can be excited independently, regardless of the appearance of primary precession.

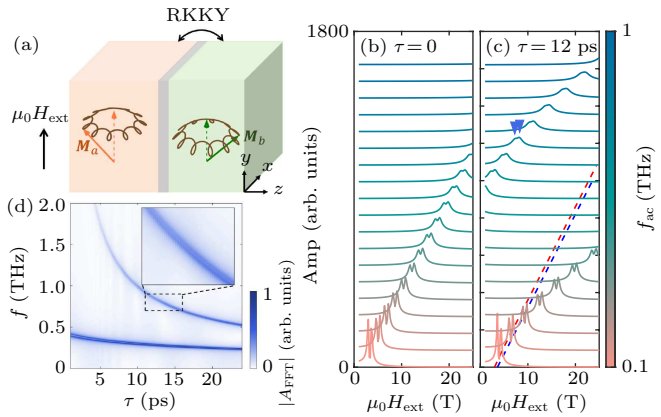


Fig. 2. (a) Schematic of magnetic moments dynamics containing nutation and precession in a synthetic FiM with magnetic moments $M_a = 3M_b$. The dashed and solid arrows represent equilibrium and instantaneous positions of magnetic moments, respectively. (b) and (c) Amplitudes of oscillating M_b^z as functions of external dc magnetic field with $\tau = 0$ and 12 ps, respectively, at the steady state in the presence of an alternating driving field $h(t) = h_0 \sin(2\pi f_{ac} t)$ at different frequencies. Results are shifted vertically for clarity. The dashed curves in (c) represent the frequency dependence of the resonance fields in (b). Two blue triangles indicate the additional resonances in the high-frequency range. (d) FFT spectrum as a function of inertial coefficient τ in $\mu_0 H_{ext} = 15$ T. The inset is an enlarged view of the dashed-line rectangle.

In order to explore the reasons behind the modification of the two low-frequency modes and the behaviors of these additional modes, we perform an alternative simulation with a sinc-function driving field $\boldsymbol{h} = h_0 \mathrm{sinc}(2\pi f_T t)\hat{x}$, where all resonances with frequencies below f_T can be equally excited simultaneously. The excitation efficiency of different modes is reflected in the fast Fourier transform (FFT) spectrum of the dynamic m_b^z component. In the simulation we take $\mu_0 h_0 =$ 10 mT and $f_T = 6$ THz to cover the frequency range of nutation modes.

Figure 2(d) shows the FFT spectrum at $\mu_0 H_{ext} = 15$ T by varying the inertial coefficient τ, from which four branches of eigenmodes are recognized. Clearly, the two lower-frequency modes indeed can be traced back to the precessional magnon modes in the limit of $\tau = 0$. The frequencies of the other two modes, however, exhibit a very quick increase with reducing τ and become divergent at a vanishing τ, reflecting the nature of nutation modes.[26] Notably, the blue shift of the modulated precession modes can be regarded as the repulsion effect from the nutation modes. The full FFT spectra calculated from sinc-function excitation at $\tau = 0$ and $\tau = 12$ ps are displayed separately in Figs. 3(a) and 3(b) as a function of external magnetic field, which agree with the features observed in Fig. 2. The nutation modes with the inclusion of the inertial term ($\tau = 12$ ps) are found to follow the magnetic field dependence of the precession modes.

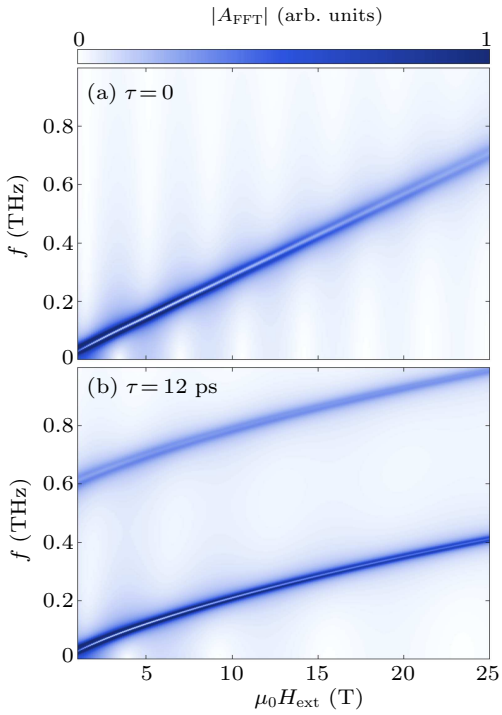


Fig. 3. FFT spectra as functions of the external magnetic field calculated from the sinc-function pulse excitation at (a) $\tau = 0$ and (b) $\tau = 12$ ps.

3.2. Mode analysis

To gain deeper insight into the magnetic moment dynamics with nutation effect, we proceed to a theoretical analysis of the resonance modes. In practice, we rewrite the ILLG equation in the frequency domain within the linear spin wave theory as

$$\omega U = \mathcal{W}_{tot} U. \tag{8}$$

The details of the derivation are provided in Appendix A, where the full expression of the dynamic matrix $\mathcal{W}_{tot}$ is written in the circular polarization basis.

Focusing on the parameters used in Fig. 3, the magnetic anisotropy is rather small compared with the external magnetic

field ($\mu_0 H_{\rm ext} \geq 1$ T), so it can be treated as a perturbation. We thus decompose the full dynamic matrix into $\mathcal{W}_{\rm tot} = \mathcal{W}_0 + \mathcal{W}'$ with

$$\mathcal{W}_0 = \begin{pmatrix} \mathcal{W}_+ & 0 \\ 0 & \mathcal{W}_- \end{pmatrix}, \tag{9}$$

and the perturbation

$$\mathcal{W}' = \begin{pmatrix} \mathcal{W}_{\rm an} & -\mathcal{W}_{\rm an} \\ -\mathcal{W}_{\rm an} & \mathcal{W}_{\rm an} \end{pmatrix}. \tag{10}$$

The specific definitions of the blocks $\mathcal{W}_\pm$ and $\mathcal{W}_{\rm an}$ are listed in Eqs. (A6) and (A7).

Note that $\mathcal{W}_+$ and $\mathcal{W}_-$ identically describe the same unperturbed modes, which can be calculated by diagonalizing one of them. Since $\alpha' \ll 1$, it is safe to further neglect α' in the term $(\mp 1 - {\rm i}\alpha')/\eta$ in Eq. (A6) for the sake of simplification. The resulting eigenvalues of $\mathcal{W}_\pm$ are obtained as

$$\omega_{\text{p-AC}} = \frac{1}{2\eta}\left[\sqrt{1+4\eta\gamma\mu_0 H_{\rm ext}} - 1\right], \tag{11}$$

$$\omega_{\text{p-OP}} = \frac{1}{2\eta}\left[\sqrt{1+4\eta\gamma(JM_{\rm tot}+\mu_0 H_{\rm ext})} - 1\right], \tag{12}$$

$$\omega_{\text{n-AC}} = \frac{-1}{2\eta}\left[\sqrt{1+4\eta\gamma\mu_0 H_{\rm ext}} + 1\right], \tag{13}$$

$$\omega_{\text{n-OP}} = \frac{-1}{2\eta}\left[\sqrt{1+4\eta\gamma(JM_{\rm tot}+\mu_0 H_{\rm ext})} + 1\right], \tag{14}$$

with $M_{\rm tot} = M_a + M_b$. The theoretical frequencies $f = \frac{|\omega|}{2\pi}$ are then plotted in Fig. 4(a) as orange curves, which show a reasonable agreement with the FFT spectra, except for a slight shift, due to the omission of $\mathcal{W}'$. The labels "p" and "n" in subscripts respectively indicate the positive and negative signs of the eigenvalues, corresponding to right- and left-handed dynamics of conventional precession and nutation with respect to the magnetic field direction in our notation. "AC" and "OP" refer to the acoustic and optical modes, respectively.

To reveal this information, we calculate the ratio of two instantaneous dynamic components from

$$r = \frac{M_a m_{a,+}}{M_b m_{b,+}} \tag{15}$$

by substituting Eqs. (11)–(14) into Eq. (A8) and obtain $r_{\text{p-OP}} = r_{\text{n-OP}} = -1$ and $r_{\text{p-AC}} = r_{\text{n-AC}} = M_a/M_b$. The negative value of $r_{\text{p(n)-OP}}$ signifies that $\boldsymbol{M}_a$ and $\boldsymbol{M}_b$ rotate out of phase, satisfying the definition of optical modes, and the unit value of $|r_{\text{p(n)-OP}}|$ means that the dynamic components of $\boldsymbol{M}_a$ and $\boldsymbol{M}_b$ are of equal amplitudes, as illustrated in Fig. 4(b). For the acoustic modes, $\boldsymbol{M}_a$ and $\boldsymbol{M}_b$ are always in the same direction, as depicted in Fig. 4(c). Since the exchange interaction favors antiparallel alignment of magnetic moments, the AC modes with parallel alignment exhibit slightly higher frequencies than the OP modes, for both nutation and precession. Notably, the frequencies of the left-handed nutation modes increase with the magnetic field, in contrast to the typical decreasing feature for left-handed precession modes with increasing magnetic field in FiMs and AFMs. The nutation and precession modes satisfy the relation $|\omega_{\text{n-OP(AC)}}| - |\omega_{\text{p-OP(AC)}}| = 1/\eta$, which explains their shared magnetic field dependence, similar to the situation in single-sublattice FMs.[26]

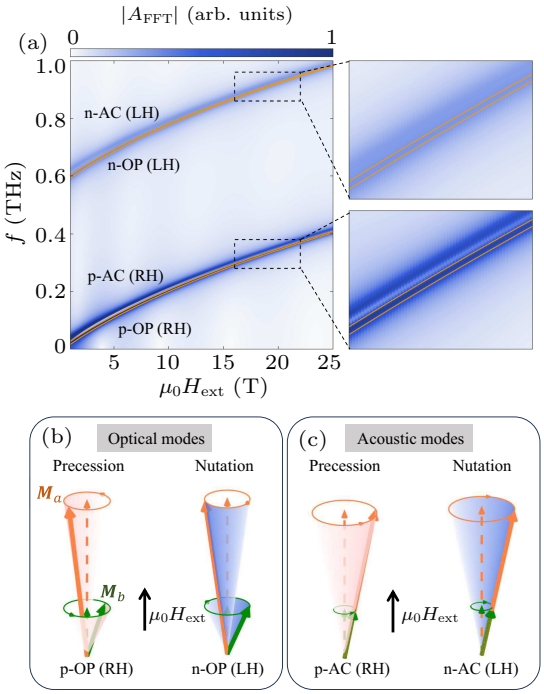


Fig. 4. (a) FFT spectra with the variation of external magnetic field at $\tau = 12$ ps, with orange curves representing theoretical results in the absence of anisotropy. Right panels show enlarged views of dashed-line rectangles in the main figure on the left. (b) and (c) Schematics of different modes.

The frequency corrections due to the magnetic anisotropy are further taken into account perturbatively, as explained in Appendix B. Specifically, we obtain

$$\omega_n' = \omega_n - \frac{\gamma(K_a M_a I_{n,n} + K_b M_b)}{(2\eta\omega_n + 1)(1 + I_{n,n})}, \tag{16}$$

with definition of $I_{n,n}$ presented in Appendix B. These corrected frequencies are plotted as red curves in Fig. 5, which are in excellent agreement with the FFT spectra from numerical simulation.

The dissipation characteristics of the eigenmodes are analyzed by directly diagonalizing the full matrix $\mathcal{W}_{\rm tot}$, where the mode frequencies and the dissipation rates can be read from the real and imaginary parts of eigenvalues, respectively. The results are plotted in Fig. 6, where all obtained frequencies increase with magnetic field, consistent with those from simulation and perturbation discussed before. On the other hand, as shown in Fig. 6(b), while the dissipation rates of the precession modes follow the magnetic field dependence of their frequencies, those of the nutation modes decrease with increasing magnetic field, in contrast to the behaviors of their

frequencies. Compared with precession modes, the systematically larger dissipation of nutation modes can be attributed to their higher frequency.

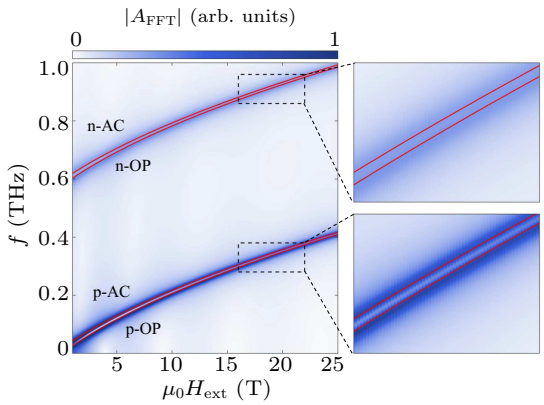


Fig. 5. Comparison of the simulated FFT spectra and the calculated frequencies from Eq. (16) with corrections due to magnetic anisotropy taken into account perturbatively. Right panels show enlarged views of dashed-line rectangles in the main figure on the left. Here, $\tau = 12$ ps.

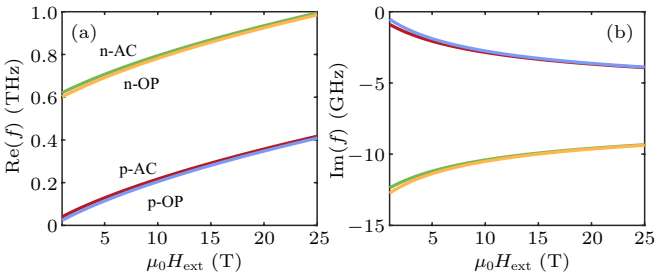


Fig. 6. (a) Real and (b) imaginary parts of eigenvalues calculated directly from the full dynamic matrix $\mathcal{W}_{\rm tot}$ as functions of external magnetic field in parallel configuration.

4. Antiparallel configuration

In the previous section regarding the parallel configuration, the precession and nutation modes are consistent with those in FMs. In order to explore the manifestation of different chiral magnons in the presence of nutation, we turn to the conventional antiparallel configuration of FiMs, as illustrated in Fig. 7(a). To stabilize this configuration over a broad range of magnetic fields requires a stronger exchange interaction. Therefore, in this part, we adopt $J = -3T/\mu_{\rm B}$, available in typical FiMs like GdIG.[41] All other parameters remain identical to those used in Section 3.

4.1. Nutation modes revealed by macromagnetic simulation

By applying the same sinusoidal alternating magnetic field as in Subsection 3.1, we simulate the magnetic resonances. Figures 7(b) and 7(c) show the variations of steady-state oscillating amplitudes during the scan of driving frequency without and with inertia at different strengths of dc external fields. In the case without inertia, i.e., $\tau = 0$, two resonance peaks are observed around 0.5 THz. When the magnetic field increases from 10 T to 20 T, the two peaks gradually merge into a single peak around 15 T, as marked by the gray triangle in Fig. 7(b), and then separate again. When the inertial term is included ($\tau = 12$ ps), two groups of resonances are observed, each containing two peaks. The two peaks in each group exhibit similar behaviors to those in Fig. 7(b), except for their weaker dependence on the field strength. The impact of the inertial term is then explicitly tracked through a systematic simulation under a pulse excitation with a sinc function with continuously varying inertial parameter τ at a fixed external magnetic field. The FFT spectrum at $\mu_0 H_{\rm ext} = 10$ T is plotted in Fig. 7(d), which shows very similar behaviors to those in Fig. 2(d). Namely, the two low-frequency modes at $\tau = 12$ ps evolve from the conventional FiM resonance modes at $\tau = 0$, while the two high-frequency modes are the nutation modes introduced by the inertia.

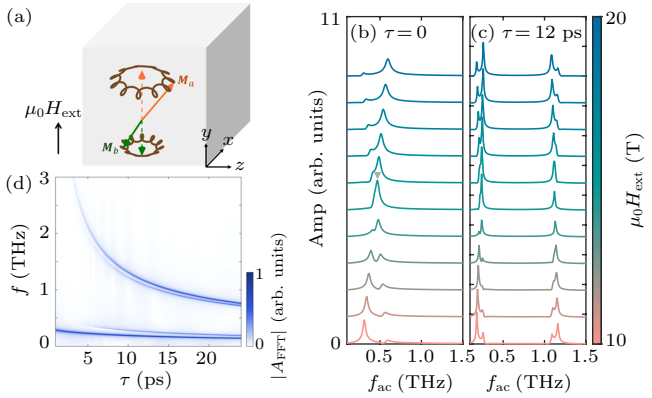


Fig. 7. (a) Schematic of magnetic dynamics affected by nutation in antiparallel configuration. (b) and (c) Amplitudes of steady-state oscillating M_b^z separately for $\tau = 0$ and 12 ps under the alternating driving field at different frequencies. Results are shifted vertically for clarity. (d) FFT spectrum of M_b^z as a function of inertial coefficient τ at $\mu_0 H_{\rm ext} = 10$ T.

The magnetic field dependencies of the resonance modes are recognized from the full FFT spectra depicted in Figs. 8(a) and 8(b), which are calculated based on sinc-function pulse excitation in the present antiparallel configuration. Without the inertial term, corresponding to $\tau = 0$ in Fig. 8(a), the frequency of $\alpha_{\rm p}$ ($\beta_{\rm p}$) increases (decreases) with magnetic field, implying its right(left)-handed characteristic. Note also that these two modes exhibit an anticrossing feature around their intersection point, which reflects the hybridization between the circular modes precessing around the magnetic field in the y direction, where the easy-plane anisotropy in the x-y plane breaks the rotational symmetry, as shown later. The relatively weaker FFT intensity of $\beta_{\rm p}$ reflects the inefficiency of the excitation because of the vanishing net dynamic magnetization of this mode, corresponding to $r = -1$ defined in Eq. (15).[42]

In the presence of the inertial term at $\tau = 12$ ps, as shown in Fig. 8(b), the two low-frequency modes, evolved from $\alpha_{\rm P}$ and $\beta_{\rm P}$ according to Fig. 7(d), still inherit the level repulsion, although their frequencies are significantly suppressed below 0.5 THz and both modes are strongly excited. Their

weak FFT strength just before the anticrossing gap is related to the strongly suppressed amplitude of m_b^z, as discussed in Appendix C. For the nutation modes α_n and β_n, it remains difficult to determine from Fig. 8(b) whether or not an anticrossing gap appears. A further discussion on this issue will be given in Subsection 4.3. Since the slope of the f–H relation reflects the gyromagnetic ratio, the comparison of the two plots in Fig. 8 [as also seen in Figs. 7(b) and 7(c)] thus suggests the suppression of the effective gyromagnetic ratio by the inertial term.

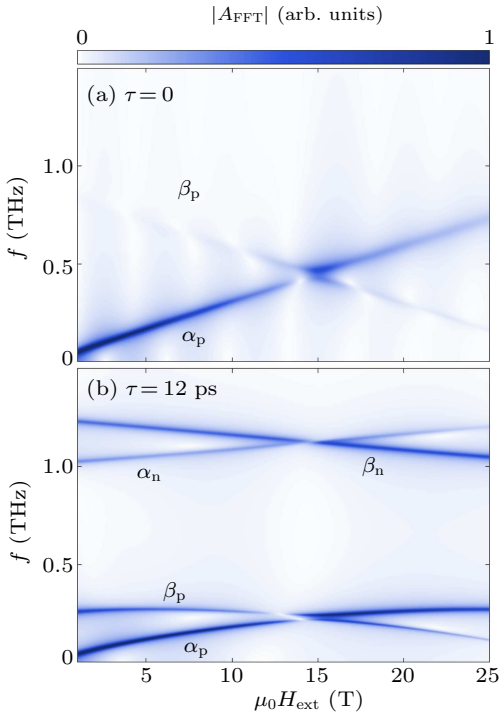


Fig. 8. FFT spectra as functions of the external magnetic field in the antiparallel configuration, calculated from the sinc-function pulse excitation at (a) $\tau = 0$ and (b) $\tau = 12$ ps.

4.2. Mode analysis without anisotropy

For theoretical analysis, we follow the perturbation procedures employed in the previous section. As a first step, we analytically calculate the eigenfrequencies of $\mathcal{W}_+$. With the detailed expression given in Appendix B, the resulting mode frequencies are plotted as black and yellow curves in Fig. 9(a), which already qualitatively describe the FFT spectrum. The vanishing of the anticrossing gap at the intersection points confirms that the hybridization in Fig. 8 remains due to the anisotropy, while the interaction between nutation and precession modes plays a marginal role.

The dynamic characteristics of the four modes are illustrated in Fig. 9(b), according to the eigenfunction of $\mathcal{W}_+$. As can be seen, the dynamic magnetic components of $\boldsymbol{M}_a$ and $\boldsymbol{M}_b$ in α_p and β_p precession modes have opposite signs, which is consistent with the conventional chiral magnons in inertia-free FiMs. In contrast, those dynamic components in the two nutation modes α_n and β_n are of the same sign, which is revealed by the positive sign of the ratio calculated from Eq. (15) and plotted in Fig. 9(c). It is noteworthy that this ratio is highly tunable by the magnetic field and deviates from -1 in general for all modes, explaining their efficient excitation.

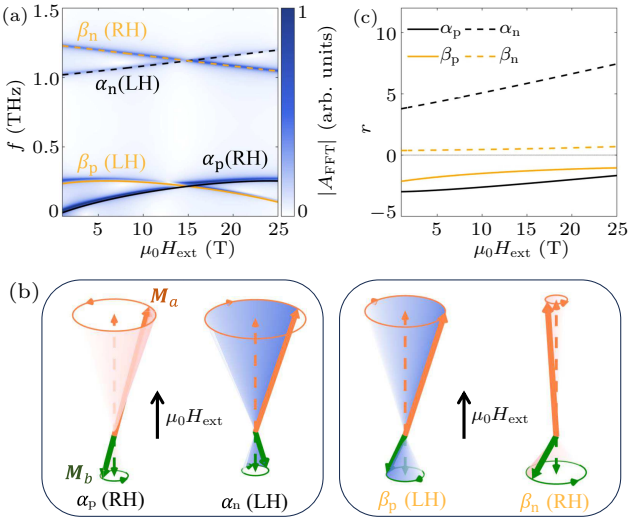


Fig. 9. (a) Comparison of the simulated FFT spectrum and the analytical solution of the frequencies calculated analytically with anisotropy excluded. (b) Schematics of different modes when $\mu_0 H_{\rm ext} = 1$ T. (c) The ratios of the two dynamic magnetic components defined as Eq. (15) as functions of external magnetic field. In this calculation, $\tau = 12$ ps.

4.3. Anisotropy-induced mode hybridization

In order to reproduce the hybridization between α_P and β_P and clarify the behavior near the intersection points between α_n and β_n, we derive the perturbation Hamiltonian of the two-level systems according to Appendix B as

$$\Omega_\xi = \begin{pmatrix} \left|\omega_{\alpha_\xi} + \delta\omega_{\alpha_\xi}\right| & V_{\alpha_\xi}^\dagger \mathcal{W}_{\rm an} U_{\beta_\xi} \\ V_{\beta_\xi}^\dagger \mathcal{W}_{\rm an} U_{\alpha_\xi} & \left|\omega_{\beta_\xi} + \delta\omega_{\beta_\xi}\right| \end{pmatrix}, \tag{17}$$

with $\xi = $ p (n) denoting precession (nutation) modes. The frequency corrections in the diagonal terms are expressed as

$$\delta\omega_n = -\frac{\gamma(K_a M_a I_{n,n} + K_b M_b)}{2\eta\omega_n(1+I_{n,n}) - 1 + I_{n,n}}, \tag{18}$$

with the quantities also provided in Appendix B.

The frequencies calculated from the diagonal terms of Eq. (17) are plotted as red curves in Figs. 10(a) and 10(b) for low- and high-frequency groups, respectively, which describe each mode quite well already, except for the level repulsion. By solving the full secular equation of Eq. (17), the eigenfrequencies are calculated and plotted in Figs. 10(c) and 10(d). While the analytical curves for α_P and β_P perfectly reproduce the FFT spectra, the curves of α_n and β_n also exhibit an anticrossing behavior. The explicit calculation gives the coupling strength

$$\Delta_\xi^2 = \frac{\gamma^2\left(K_a M_a I_{\alpha_\xi,\beta_\xi} + K_b M_b\right)^2}{\alpha_\xi,\beta_\xi - \prod_\varepsilon \left[2\eta\omega_\varepsilon(1+I_{\varepsilon,\varepsilon}) - 1 + I_{\varepsilon,\varepsilon}\right]}, \tag{19}$$

with specific definitions listed in Appendix B. By substituting the parameters, the coupling strengths are found to be $\Delta_{\rm p} \simeq 12$ GHz and $\Delta_{\rm n} \simeq 2.5$ GHz. The dependences of $\Delta_{\rm p}$ and $\Delta_{\rm n}$ on τ are further discussed in Appendix D.

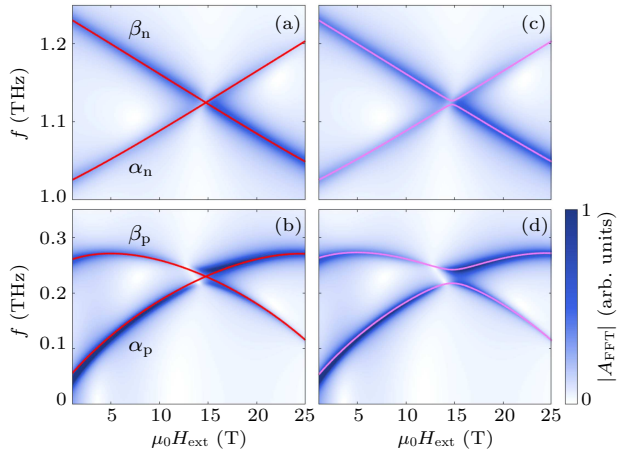


Fig. 10. Comparison of simulated FFT spectra at $\tau = 12$ ps and the theoretical curves with anisotropy included perturbatively in Eq. (17). Red curves in (a) and (b) are the plots of the diagonal terms. Pink curves in (c) and (d) are obtained from the full Eq. (17).

Figures 11(a) and 11(b) show the real and imaginary parts of the eigenvalues numerically calculated from the full $\mathcal{W}_{\rm tot}$. As expected, the magnetic field dependence of the real part is consistent with that in Fig. 8(b). For the imaginary part, one can see that the dissipation of the higher precession mode becomes comparable to that of the nutation modes even though they have a big difference in frequency. This is another consequence of the strong interaction between precession modes and nutation ones. As a general feature for the dissipation of all modes in the antiparallel configuration, a higher frequency gives a larger dissipation, which is different from that in the parallel configuration. From Fig. 11(b), the dissipation rates of the nutation modes are about 8 GHz, much larger than $\Delta_{\rm n}$, explaining the absence of anticrossing behavior between $\alpha_{\rm n}$ and $\beta_{\rm n}$ in Fig. 8 with the parameters adopted in the present simulation.

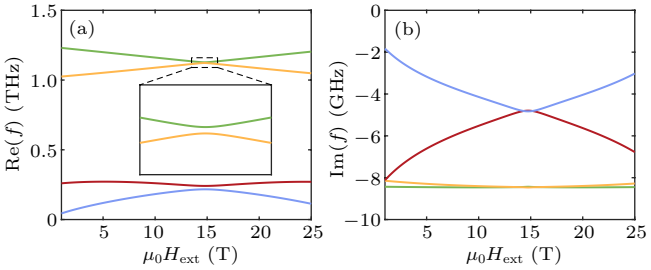


Fig. 11. (a) Real and (b) imaginary parts of eigenvalues calculated directly from the full dynamic matrix $\mathcal{W}_{\rm tot}$ as functions of external magnetic field in antiparallel configuration.

According to Eq. (19), the coupling between nutation modes is proportional to the anisotropy strength. In order to clearly display their anticrossing feature, a larger anisotropy $K_a = K_b = -0.5T/\mu_{\rm B}$ is adopted with other parameters unchanged. The results are plotted in Fig. 12(a), which indeed exhibits a visible gap. In this case, the coupling strength of nutation modes estimated from Eq. (19) is around 24 GHz, larger than the corresponding linewidth of around 8 GHz shown in Fig. 12(b).

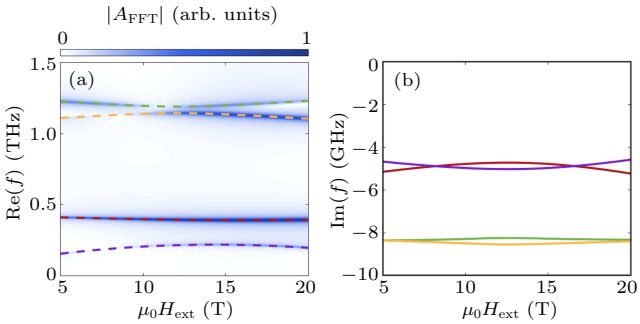


Fig. 12. (a) The FFT spectrum as a function of external magnetic field with $K_a = K_b = -0.5T/\mu_{\rm B}$ and $\tau = 12$ ps. The dashed curves in (a) are real part of eigenvalues calculated directly from the full dynamic matrix with imaginary part plotted in (b).

5. Conclusion

In summary, we studied the effects of nutation on magnetic resonance in FiMs based on the ILLG equation of two antiferromagnetically coupled macromagnetic moments, where the inertial term generates two nutation modes, which show general features in both parallel and antiparallel configurations of the two macromagnetic moments. We found that the nutation modes can be excited independently, resulting in resonance peaks during the field sweeping at a fixed frequency or the frequency sweeping at a fixed magnetic field. Therefore, nutation modes can be detected by THz magnon spectroscopy, in addition to the time-resolved magneto-optical Kerr effect technique used in Refs. [36–38]. While the frequencies of such nutation modes decrease with increasing inertial coefficient, they also considerably reduce the frequency of the precession modes, showing a level repulsion between the nutation and the precession modes. Such an effect is also reflected in the modulation of the effective gyromagnetic ratio in the magnetic field dependence of resonance frequencies. On the other hand, the nutation modes in the two configurations exhibit distinct behaviors in dissipation and mode hybridization. In addition, we developed a perturbation method to reproduce the numerical results, which not only helps to clarify the opposite chirality of the nutation in comparison to the corresponding conventional precession modes in each configuration, but also allows a quantitative description of the anticrossing gap resulting from the mode hybridization between chiral magnons in the antiparallel configuration.

Appendix A: Derivation of dynamic matrix

In this appendix, we derive the dynamic matrix from the revised ILLG equation in Eqs. (5) and (6). Assuming the equilibrium magnetization in the y direction, we apply linear ex-

pansion to the normalized magnetic moment

$$\begin{aligned} \boldsymbol{m}_a &= \hat{y} + (m_{a,x}\hat{x} + m_{a,z}\hat{z})\, \mathrm{e}^{-\mathrm{i}\omega t}, \\ \boldsymbol{m}_b &= c\hat{y} + \left(m_{b,x}\hat{x} + m_{b,z}\hat{z}\right) \mathrm{e}^{-\mathrm{i}\omega t}, \end{aligned} \tag{A1}$$

with $|m_{a(b),x(z)}| \ll 1$, where $c = +1$ (-1) for the parallel (antiparallel) configuration. Similarly, the auxiliary vectors are expressed as

$$\boldsymbol{g}_i = (g_{i,x}\hat{x} + g_{i,z}\hat{z})\, \mathrm{e}^{-\mathrm{i}\omega t}, \tag{A2}$$

with subscript $i = a, b$. In the representation of circular polarization,

$$\begin{aligned} m_{i,\pm} &= m_{i,z} \pm \mathrm{i} m_{i,x}, \\ g_{i,\pm} &= g_{i,z} \pm \mathrm{i} g_{i,x}. \end{aligned} \tag{A3}$$

The full basis space is defined as $U = \left(U_+^{\mathrm{T}}, U_-^{\mathrm{T}}\right)^{\mathrm{T}}$, with $U_\pm = \left(g_{a,\pm}, m_{a,\pm}, g_{b,\pm}, m_{b,\pm}\right)^{\mathrm{T}}$. Equations (5) and (6) then can be rewritten as

$$\omega U = \mathcal{W}_{\mathrm{tot}} U, \tag{A4}$$

where

$$\mathcal{W}_{\mathrm{tot}} = \begin{pmatrix} \mathcal{W}_+ + \mathcal{W}_{\mathrm{an}} & -\mathcal{W}_{\mathrm{an}} \\ -\mathcal{W}_{\mathrm{an}} & \mathcal{W}_- + \mathcal{W}_{\mathrm{an}} \end{pmatrix}, \tag{A5}$$

with

$$\mathcal{W}_\pm = \begin{pmatrix} \mp\frac{1}{\eta} - \frac{\mathrm{i}\alpha'}{\eta} & \mathcal{A} & 0 & \mathrm{i}\gamma J M_b \\ \mathrm{i}\frac{1}{\eta} & 0 & 0 & 0 \\ 0 & \mathrm{i}\gamma J M_a & \mp c\frac{1}{\eta} - \frac{\mathrm{i}\alpha'}{\eta} & \mathcal{B} \\ 0 & 0 & \mathrm{i}\frac{1}{\eta} & 0 \end{pmatrix}, \tag{A6}$$

$$\mathcal{W}_{\mathrm{an}} = \begin{pmatrix} 0 & \mathrm{i}\gamma K_a M_a & 0 & 0 \\ 0 & 0 & 0 & 0 \\ 0 & 0 & 0 & \mathrm{i}\gamma K_b M_b \\ 0 & 0 & 0 & 0 \end{pmatrix}. \tag{A7}$$

In Eq. (A6), we define $\mathcal{A} = -\mathrm{i}\gamma(cJM_b + \mu_0 H_{\mathrm{ext}})$ and $\mathcal{B} = -\mathrm{i}\gamma c\,(JM_a + \mu_0 H_{\mathrm{ext}})$. By neglecting the small α' in Eq. (A6), we can calculate the ratio between the two dynamic components of $\boldsymbol{M}_a$ and $\boldsymbol{M}_b$ as

$$r = \frac{M_a m_{a,\pm}}{M_b m_{b,\pm}} = \frac{\gamma J M_a}{\gamma(cJM_b + \mu_0 H_{\mathrm{ext}}) - \omega - \eta\omega^2}. \tag{A8}$$

Appendix B: Details of perturbation calculation

Since the anisotropy is weak in this study, $\mathcal{W}_{\mathrm{an}}$ is treated perturbatively. The main part of dynamic matrix ($\mathcal{W}_0$) is a diagonalizable non-Hermitian matrix. By employing techniques from the linear algebra, we calculate the eigenvectors U_n and V_n from $\mathcal{W}_0$ and $\mathcal{W}_0^\dagger$, respectively, which share the same eigenvalues ω_n. These eigenvectors satisfy the orthonormality condition

$$V_m^\dagger U_n = \delta_{m,n}. \tag{B1}$$

The matrix element of the perturbation Hamiltonian $\mathcal{W}_{\mathrm{an}}$ is then given by

$$\delta\omega_{mn} = V_{+,m}^\dagger \mathcal{W}_{\mathrm{an}} U_{+,n}. \tag{B2}$$

Following some straightforward calculations, we obtain the correction to the diagonal element

$$\delta\omega_n = \frac{-\gamma(K_a M_a I_{n,n} + K_b M_b)}{2\eta\omega_n(1 + I_{n,n}) + c + I_{n,n}}, \tag{B3}$$

which depends on the choice of c, reflecting the difference between parallel and antiparallel configurations. In Eqs. (B3) and (19), we define $I_{m,n} = M_a M_b l_m l_n$ with

$$l_{m(n)} = \frac{-\gamma J}{-\gamma(cJM_b + \mu_0 H_{\mathrm{ext}}) + \omega_{m(n)} + \eta\omega_{m(n)}^2}. \tag{B4}$$

Specified to the antiparallel configuration with $c = -1$, we have

$$\omega_{\alpha_{\mathrm{p}}} = (a_4 - \sqrt{-a_4^2 - a_2 a_4 - a_1\sqrt{a_4/2}})/\sqrt{2a_4}, \tag{B5}$$

$$\omega_{\beta_{\mathrm{p}}} = -(a_4 - \sqrt{-a_4^2 - a_2 a_4 + a_1\sqrt{a_4/2}})/\sqrt{2a_4}, \tag{B6}$$

$$\omega_{\alpha_{\mathrm{n}}} = -(a_4 + \sqrt{-a_4^2 - a_2 a_4 + a_1\sqrt{a_4/2}})/\sqrt{2a_4}, \tag{B7}$$

$$\omega_{\beta_{\mathrm{n}}} = (a_4 + \sqrt{-a_4^2 - a_2 a_4 - a_1\sqrt{a_4/2}})/\sqrt{2a_4}, \tag{B8}$$

where

$$\begin{aligned} a_4 &= \left[-a_3 + \sqrt{a_3^2 + \left(-a_2^2/36 - a_0/3\right)^3}\right]^{\frac{1}{3}} \\ &\quad + \left[-a_3 - \sqrt{a_3^2 + \left(-a_2^2/36 - a_0/3\right)^3}\right]^{\frac{1}{3}} - a_2/3, \\ a_3 &= -a_2^3/216 + a_0 a_2/6 - a_1^2/16, \\ a_2 &= [\gamma\eta J(M_a + M_b) - 1]/\eta^2, \\ a_1 &= \gamma[J(M_a - M_b) + 2\mu_0 H_{\mathrm{ext}}]/\eta^2, \\ a_0 &= -\gamma^2\mu_0 H_{\mathrm{ext}}[J(M_a - M_b) + \mu_0 H_{\mathrm{ext}}]/\eta^2. \end{aligned}$$

The signs of $\omega_{\alpha_{\mathrm{p}}}$ and $\omega_{\beta_{\mathrm{n}}}$ are positive representing right-handed polarization, while the negative signs of $\omega_{\beta_{\mathrm{p}}}$ and $\omega_{\alpha_{\mathrm{n}}}$ indicate left-handed rotation of magnetic moments about the magnetic field.

Appendix C: Hybridization feature between chiral modes

In the FFT spectra of Figs. 8–11, some "white gaps" appear near the anticrossing gap, labeled as "B" and "E" points in Fig. C1(a), which is related to the strongly suppressed amplitude of m_b^z as shown in Fig. C1(b). The suppression appears approximately at the transition of left- and right-handed modes, reflecting the hybridization between chiral modes.

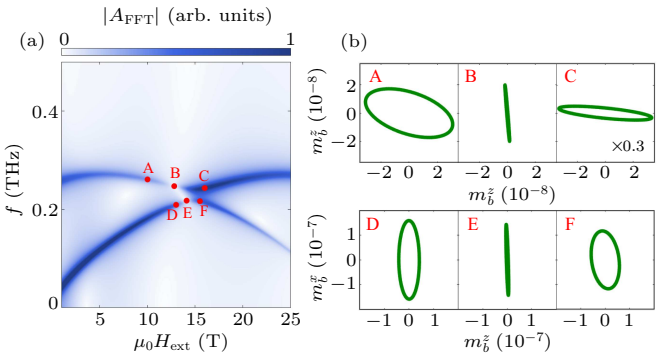


Fig. C1. (a) The FFT spectrum as a function of external magnetic field in the antiparallel phase with $\tau = 12$ ps and $K_a = K_b = -0.05T/\mu_{\rm B}$. (b) The mode trajectories of m_b with corresponding magnetic field and frequency labeled in (a).

Appendix D: The influence of inertial coefficient on the hybridization

The magnetic field at the anticrossing gap (or the intersection point in the absence of mode hybridization), i.e., $\mu_0 H_{\rm ext}^{\rm g}$, is defined according to $\left|\omega_{\alpha_\xi} + \delta\omega_{\alpha_\xi}\right| = \left|\omega_{\beta_\xi} + \delta\omega_{\beta_\xi}\right|$. Figure D1(a) shows that $\mu_0 H_{\rm ext}^{\rm g}$ is insensitive to τ for both precession and nutation modes. According to Eq. (19), the coupling strength is calculated with different inertial coefficient and shown in Fig. D1(b). As τ increases, the coupling strength of nutation modes first increases and then decreases, while that of precession modes monotonically declines.

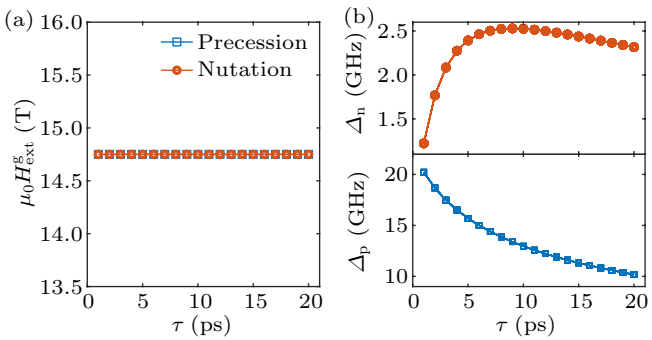


Fig. D1. (a) The magnetic field and (b) the coupling strength corresponding to the gap of precession and nutation modes as functions of inertial coefficient τ.

The influence of τ in Eq. (19) could be introduced by I_{α_ξ,β_ξ} in the numerator, as well as $\eta\omega_{\alpha_\xi}$ ($\eta\omega_{\beta_\xi}$) and $I_{\alpha_\xi,\alpha_\xi}$ (I_{β_ξ,β_ξ}) terms in the denominator. As shown in Fig. D2(a), I_{α_ξ,β_ξ} only slightly differs from 1 during the variation of τ and therefore can be regarded as a constant, i.e., $I_{\alpha_\xi,\beta_\xi} = 1$. The τ dependence of Δ_ξ is thus dominated by $\eta\omega_{\alpha_\xi}$ ($\eta\omega_{\beta_\xi}$) and $I_{\alpha_\xi,\alpha_\xi}$ (I_{β_ξ,β_ξ}), which are plotted in Figs. D2(b) and D2(c), respectively. For the precession modes, $I_{\alpha_{\rm p},\alpha_{\rm p}}$ and $I_{\beta_{\rm p},\beta_{\rm p}}$ have relatively weak dependency on τ, and can be respectively assumed as constants $I^0_{\alpha_{\rm p},\alpha_{\rm p}}$ and $I^0_{\beta_{\rm p},\beta_{\rm p}}$. Considering the conditions of $\eta\omega_{\alpha_{\rm p}} > 0$, $I_{\alpha_{\rm p},\alpha_{\rm p}} > 1$, $\eta\omega_{\beta_{\rm p}} < 0$, and $0 < I_{\beta_{\rm p},\beta_{\rm p}} < 1$, Eq. (19) leads to

$$\Delta_{\rm p}^2 \approx \frac{\gamma^2 \left(K_a M_a + K_b M_b\right)^2}{\left[2\left|\eta\omega_{\alpha_{\rm p}}\right|\left(1 + I^0_{\alpha_{\rm p},\alpha_{\rm p}}\right) + \left(I^0_{\alpha_{\rm p},\alpha_{\rm p}} - 1\right)\right]\left[2\left|\eta\omega_{\beta_{\rm p}}\right|\left(1 + I^0_{\beta_{\rm p},\beta_{\rm p}}\right) + \left(1 - I^0_{\beta_{\rm p},\beta_{\rm p}}\right)\right]}, \tag{D1}$$

which decreases monotonically as the magnitudes of $\eta\omega_{\alpha_{\rm p}}$ and $\eta\omega_{\beta_{\rm p}}$ both increase with τ, consistent with the numerical results plotted in Fig. D1(b). For the nutation modes, $I_{\beta_{\rm n},\beta_{\rm n}}$ is very small and can be neglected. With the further consideration of $-2\eta\omega_{\alpha_{\rm n}} > 1$ and $2\eta\omega_{\beta_{\rm n}} > 1$, Eq. (19) specified to the nutation case can be expressed as

$$\Delta_{\rm n}^2 \approx \frac{\gamma^2 \left(K_a M_a + K_b M_b\right)^2}{\left[I_{\alpha_{\rm n},\alpha_{\rm n}}\left(-2\eta\omega_{\alpha_{\rm n}} - 1\right) - 2\eta\omega_{\alpha_{\rm n}} + 1\right]\left(2\eta\omega_{\beta_{\rm n}} - 1\right)}. \tag{D2}$$

In the small τ region, $I_{\alpha_{\rm n},\alpha_{\rm n}}$ has a large value and decreases drastically with increasing τ, which dominates the τ dependence and leads to the increase of $\Delta_{\rm n}$ shown in Fig. D1(b). In the large τ region, the variation of $I_{\alpha_{\rm n},\alpha_{\rm n}}$ becomes relatively slow. As a result, the increasing magnitudes of $\eta\omega_{\alpha_{\rm n}}$ and $\eta\omega_{\beta_{\rm n}}$ dominate the variation of $\Delta_{\rm n}$, which exhibits a decreasing feature with increasing τ.

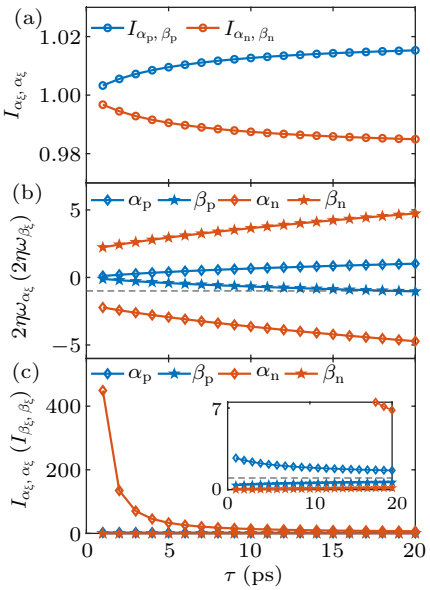


Fig. D2. (a) I_{α_ξ,β_ξ}, (b) $2\eta\omega_{\alpha_\xi}$ ($2\eta\omega_{\beta_\xi}$) and (c) $I_{\alpha_\xi,\alpha_\xi}$ (I_{β_ξ,β_ξ}) as functions of τ. The dashed lines in (b) and (c) respectively mark the positions of -1 and 1. The inset in (c) is an enlarged view.

Acknowledgements

This work was supported by the National Natural Science Foundation of China (Grant No. 12374100) and the Fundamental Research Funds for the Central Universities.

References

[1] Jungwirth T, Marti X, Wadley P and Wunderlich J 2016 *Nat. Nanotechnol.* **11** 231
[2] Kim S K, Beach G S D, Lee K J, Ono T, Rasing T and Yang H 2022 *Nat. Mater.* **21** 24
[3] Cui J, Boström E V, Ozerov M, Wu F, Jiang Q, Chu J H, Li C, Liu F, Xu X, Rubio A and Zhang Q 2023 *Nat. Commun.* **14** 3396
[4] Sukhanov A S, Utesov O I, Korshunov A N, Andriushin N D, Pavlovskii M S, Nikitin S E, Kulbakov A A, Manna K, Felser C and Rahn M C 2025 *Phys. Rev. Lett.* **135** 086703
[5] Zhang X, Galda A, Han X, Jin D and Vinokur V M 2020 *Phys. Rev. Appl.* **13** 044039
[6] Li Y, Wang W, Liu C, Chen A, Zheng D, Yang T, Tang M, Fang B, Ma Y, Shen K, Manchon A, Qiu Z and Zhang X 2025 *Adv. Mater.* **37** 2416190
[7] Wang W and Shen K 2025 *Phys. Rev. B* **111** 094413
[8] Liu Y, Xu Z, Liu L, Zhang K, Meng Y, Sun Y, Gao P, Zhao H W, Niu Q and Li J 2022 *Nat. Commun.* **13** 1264
[9] Zhang Y, Qiu L, Chen J, Wu S, Wang H, Malik I A, Cai M, Wu M, Gao P, Hua C, Yu W, Xiao J, Jiang Y, Yu H, Shen K and Zhang J 2025 *Nat. Mater.* **24** 69
[10] Kim C, Lee S, Kim H G, Park J H, Moon K W, Park J Y, Yuk J M, Lee K J, Park B G, Kim S K, Kim K J and Hwang C 2020 *Nat. Mater.* **19** 980
[11] Li Y, Zheng D, Fang B, Liu C, Zhang C, Chen A, Ma Y, Shen K, Liu H, Manchon A and Zhang X 2022 *Adv. Mater.* **34** 2200019
[12] Wang L, Shen L, Bai H, Zhou H A, Shen K and Jiang W 2024 *Phys. Rev. Lett.* **133** 166705
[13] Liang J J, Xi X K, Wang W H and Lau Y C 2024 *Chin. Phys. B* **33** 077504
[14] Duan Y, Cong A and Shen K 2025 *Phys. Rev. Appl.* **23** L051006
[15] Li K, Wang L, Wang Y, Guo Y, Lv S, He Y, Lin W, Min T, Hu S, Yang S, Xue D, Zheng A, Yang S and Ding X 2024 *Adv. Mater.* **36** 2312137
[16] Huang X, Chen X, Li Y, Mangeri J, Zhang H, Ramesh M, Taghinejad H, Meisenheimer P, Caretta L, Susarla S, Jain R, Klewe C, Wang T, Chen R, Hsu C H, Harris I, Husain S, Pan H, Yin J, Shafer P, Qiu Z, Rodrigues D R, Heinonen O, Vasudevan D, Íñiguez J, Schlom D G, Salahuddin S, Martin L W, Analytis J G, Ralph D C, Cheng R, Yao Z and Ramesh R 2024 *Nat. Mater.* **23** 898
[17] Yu W, Lan J and Xiao J 2020 *Phys. Rev. Appl.* **13** 024055
[18] Jia C, Chen M, Schäffer A F and Berakdar J 2021 *npj Comput. Mater.* **7** 101
[19] Qian J, Hong Q, Wang Z Y, Wu W X, Yang Y, Hu C M, You J Q and Wang Y P 2025 *Nat. Commun.* **16** 8100
[20] Landau L and Lifshitz E 1992 *Perspectives in Theoretical Physics* (Amsterdam: Pergamon) pp. 51–65
[21] Gilbert T 2004 *IEEE Trans. Magn.* **40** 3443
[22] Ciornei M C, Rubí J M and Wegrowe J E 2011 *Phys. Rev. B* **83** 020410
[23] Fähnle M, Steiauf D and Illg C 2011 *Phys. Rev. B* **84** 172403
[24] Wegrowe J E and Ciornei M C 2012 *Am. J. Phys.* **80** 607
[25] Mondal R, Berritta M and Oppeneer P M 2018 *J. Phys.: Condens. Matter* **30** 265801
[26] Mondal R, Großenbach S, Rózsa L and Nowak U 2021 *Phys. Rev. B* **103** 104404
[27] Winter L, Großenbach S, Nowak U and Rózsa L 2022 *Phys. Rev. B* **106** 214403
[28] Li Y, Naletov V V, Klein O, Prieto J L, Muñoz M, Cros V, Bortolotti P, Anane A, Serpico C and de Loubens G 2019 *Phys. Rev. X* **9** 041036
[29] Cherkasskii M, Farle M and Semisalova A 2020 *Phys. Rev. B* **102** 184432
[30] Angster D, Dannegger T, Schlegel J, Evers M and Nowak U 2025 *Sci. Rep.* **15** 21543
[31] Titov S V, Dowling W J and Kalmykov Y P 2022 *J. Appl. Phys.* **131** 193901
[32] Makhfudz I, Olive E and Nicolis S 2020 *Appl. Phys. Lett.* **117** 132403
[33] Titov S V, Dowling W J, Kalmykov Y P and Cherkasskii M 2022 *Phys. Rev. B* **105** 214414
[34] Mondal R and Rózsa L 2022 *Phys. Rev. B* **106** 134422
[35] Cherkasskii M, Farle M and Semisalova A 2021 *Phys. Rev. B* **103** 174435
[36] Neeraj K, Awari N, Kovalev S, Polley D, Zhou Hagström N, Arekapudi S S P K, Semisalova A, Lenz K, Green B, Deinert J C, Ilyakov I, Chen M, Bawatna M, Scalera V, d'Aquino M, Serpico C, Hellwig O, Wegrowe J E, Gensch M and Bonetti S 2021 *Nat. Phys.* **17** 245
[37] Unikandanunni V, Medapalli R, Asa M, Albisetti E, Petti D, Bertacco R, Fullerton E E and Bonetti S 2022 *Phys. Rev. Lett.* **129** 237201
[38] De A, Schlegel J, Lentfert A, Scheuer L, Stadtmüller B, Pirro P, von Freymann G, Nowak U and Aeschlimann M 2025 *Phys. Rev. B* **111** 014432
[39] Sud A, Yamamoto K, Suzuki K Z, Mizukami S and Kurebayashi H 2023 *Phys. Rev. B* **108** 104407
[40] Wang Y, Zhang Y, Li C, Wei J, He B, Xu H, Xia J, Luo X, Li J, Dong J, He W, Yan Z, Yang W, Ma F, Chai G, Yan P, Wan C, Han X and Yu G 2024 *Nat. Commun.* **15** 2077
[41] Li S, Shen K and Xia K 2020 *Phys. Rev. B* **102** 224413
[42] Hsu W H, Shen K, Fujii Y, Koreeda A and Satoh T 2020 *Phys. Rev. B* **102** 174432